

Charge-integrating organic heterojunction phototransistors for wide-dynamic-range image sensors

Adrien Pierre*, Abhinav Gaikwad and Ana Claudia Arias

Solution-processed phototransistors can substantially advance the performance of image sensors. Phototransistors exhibit large photoconductive gain and a sublinear responsivity to irradiance, which enables a logarithmic sensing of irradiance that is akin to the human eye and has a wider dynamic range than photodiode-based image sensors. Here, we present a novel solution-processed phototransistor composed of a heterostructure between a high-mobility organic semiconductor and an organic bulk heterojunction. The device efficiently integrates photogenerated charge during the period of a video frame then quickly discharges it, which significantly increases the signal-to-noise ratio compared with sampling photocurrent during readout. Phototransistor-based image sensors processed without photolithography on plastic substrates integrate charge with external quantum efficiencies above 100% at 100 frames per second. In addition, the sublinear responsivity to irradiance of these devices enables a wide dynamic range of 103 dB at 30 frames per second, which is competitive with state-of-the-art image sensors.

Printed electronics allow the fabrication of inexpensive, large-area and distributed optoelectronics for health monitoring^{1,2} and energy harvesting³. Printable photodetectors, including phototransistors and photodiodes, have potential for the creation of low-cost but high-performance image sensors on flexible substrates^{4–12}, and could open new methods of imaging not possible with rigid substrates^{13,14}. Phototransistors produce photoconductive gain, which is not seen in photodiodes, and results in external quantum efficiencies (EQEs) well over 100% (refs 15–20). These devices also have a sublinear responsivity (decreasing EQE) to irradiance^{5,21}, as opposed to the linearity (constant EQE) of photodiodes⁵. Figure 1a compares the charge output, as a function of irradiance, from an image sensor pixel for a photodiode and a phototransistor. In low lighting, photoconductive gain in the phototransistor enables higher EQEs than the photodiode-based pixel. The sublinear responsivity of phototransistors to irradiance prevents photogenerated charge from saturating the charge capacity of the photodetector in the pixel (well capacity) or readout circuitry at high irradiances. The combination of photoconductive gain and sublinear responsivity of a phototransistor-based pixel leads to a wider dynamic range than a photodiode-based pixel.

Intra-pixel integration of photogenerated charge is necessary to achieve a high signal-to-noise ratio (SNR) at video frame rates. Figure 1b illustrates the rolling shutter addressing scheme used in most consumer image sensors^{22,23}, in which charge is integrated in the pixel starting at the beginning of the frame. The integrated charge from each pixel in a row of the array is simultaneously read out from the column lines as each row is scanned. The SNR of the integrated charge is substantially larger than the instantaneous photocurrent when scanning each row. Up to now, only monolithically integrated solution-processed organic photodiodes (OPDs) and thin-film transistors (TFTs) have been shown to operate at video frame rates, which are on the order of 30 frames per second (f.p.s.)^{9,24,25}. Monolithic integration of OPDs and TFTs is complicated by differences in geometries, electrodes and active

layers, and requires heterogeneous assembly. On the other hand, a phototransistor capable of charge integration^{18,26} and a fast response time^{17,27,28} can operate at higher efficiencies, have a wider dynamic range, and simplify pixel fabrication. Previous developments in high-detectivity solution-processed phototransistors for image sensing show high EQEs using direct photocurrent sampling^{15,19,29} or integration on the order of seconds^{18,26}. However, none has been shown to integrate photogenerated charge at video frame rates.

An array of pixels that is addressable and readable from external components is required for image sensors. Using the same deposited source–drain and gate electrodes as read and address lines, respectively, and a gate dielectric layer between these lines, simplifies the fabrication process and is commonplace for both lithographically processed^{10,15,19,26,29,30} and printed device arrays^{31–33}. However, highly resistive read lines may result from source–drain electrodes typically not being optimized for conductivity but rather for charge injection and extraction from the semiconductor. Additionally, the gate dielectric is optimized for high areal capacitance to increase the transconductance of the pixel, resulting in high parasitic capacitances where address and read lines overlap. The high resistance and capacitance of these lines slows scan rates and causes parasitic charge injection, which raises the noise floor of a pixel's signal²³.

Here, we demonstrate solution-processed image sensors on plastic substrates processed without photolithography, using a novel phototransistor architecture based on an organic heterostructure of a high-mobility semiconductor deposited on a mixed donor–acceptor bulk heterojunction (BHJ). These devices show a mean mobility of $1.47 \text{ cm}^2 \text{ V}^{-1} \text{ s}^{-1}$, an on–off ratio of over 1×10^5 , and EQEs above 1,200% in the on state. Image sensors are formed by screen-printing address and read lines on top of an array of discrete devices to reduce the resistance and parasitic capacitance of the read and address lines. The fast readout time and photoconductive gain of the phototransistors enables charge integration at frame rates up to 100 f.p.s. with EQEs over 100% at irradiances below $1 \mu\text{W cm}^{-2}$

Department of Electrical Engineering and Computer Sciences, University of California Berkeley, Berkeley, California 94720, USA.

*e-mail: adrien.pierre@parc.com

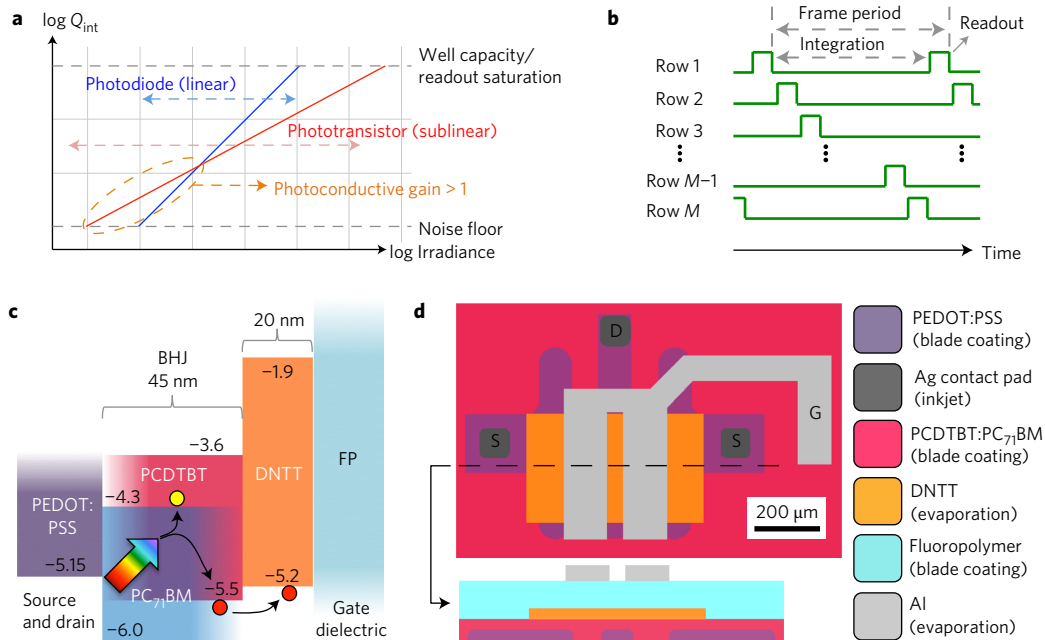


Figure 1 | Image sensing and phototransistor device architecture. **a**, Dynamic range of integrated charge for a pixel using a photodiode (linear responsivity) and a phototransistor (sublinear responsivity with photoconductive gain). **b**, Rolling shutter row-addressing scheme used in commercial image sensors for integration and readout of photogenerated charge during a frame period. **c**, Band diagram of the phototransistor device showing the migration of a photogenerated hole from the PCDTBT:PC₇₁BM donor-acceptor BHJ to the high-mobility semiconductor DNTT. **d**, Schematic and cross-sectional view of the phototransistor device and a chronological list of all deposited layers.

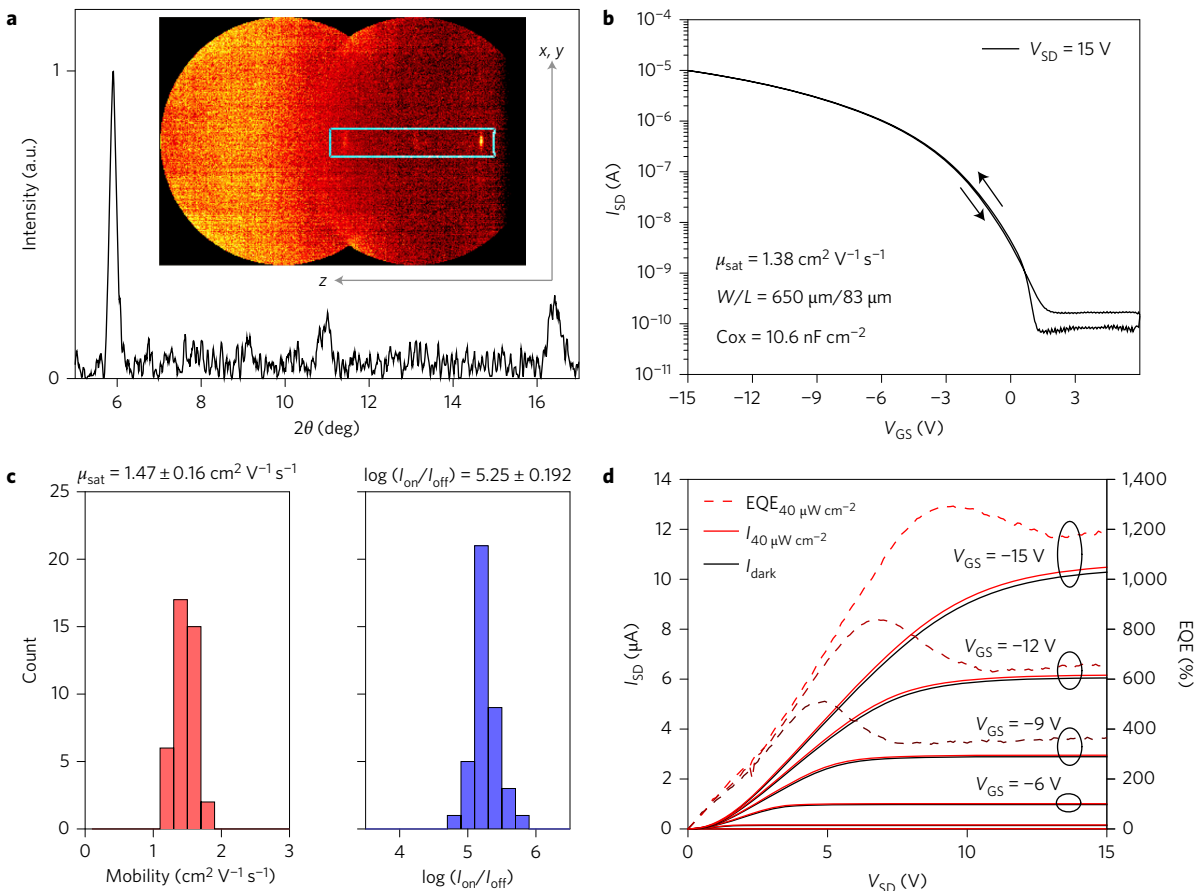


Figure 2 | Phototransistor quasi-static device performance. **a**, X-ray diffraction peaks of DNTT film on PCDTBT:PC₇₁BM. **b**, Dark transfer characteristic of a phototransistor for forward and backward sweeps at a rate of 5 V s^{-1} . **c**, Statistical variability of mobility and on-off ratio for 40 devices. **d**, Output characteristics and EQE of a phototransistor in the dark and under an irradiance of $40 \mu\text{W cm}^{-2}$ at 532 nm.

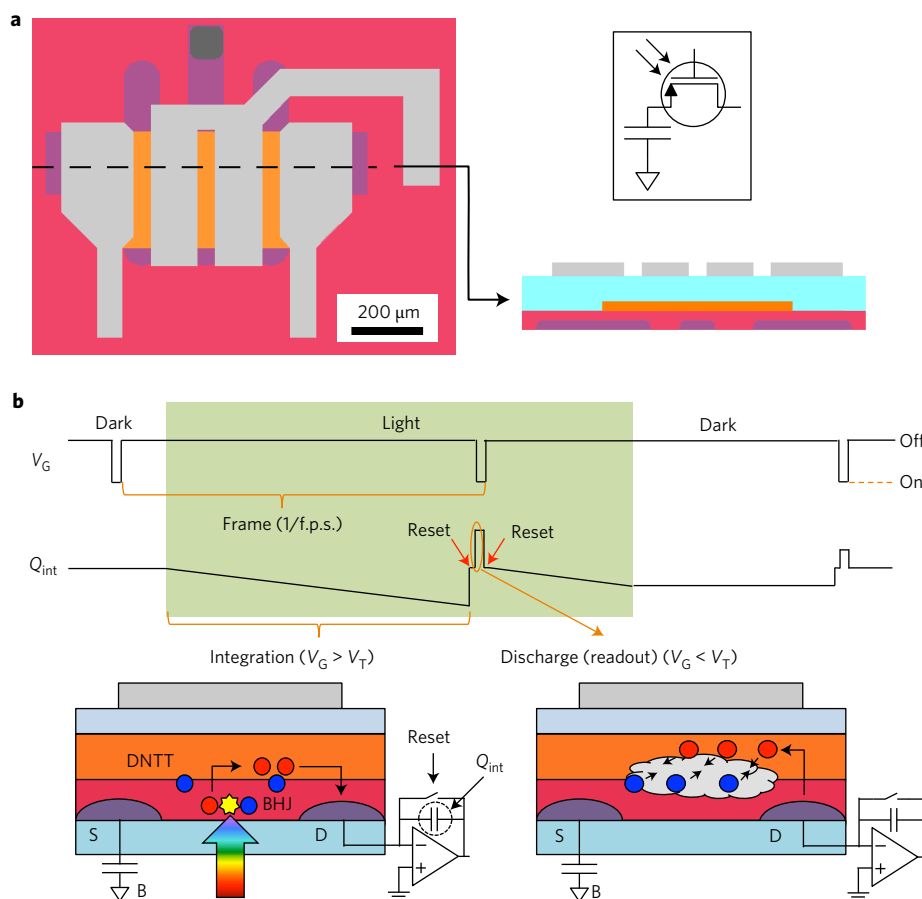


Figure 3 | Phototransistor-based pixel architecture and operation. **a**, Schematic and cross-sectional view of phototransistor-based pixel. **b**, Drive (V_G) and readout (Q_{int}) scheme of pixel operation. The first phase and vast majority of the frame period is charge integration of electrons (blue) followed by a fast discharge of the electrons through recombination with injected holes (red) to quickly read out the signal.

at 532 nm. A dynamic range of 103 dB at 30 f.p.s. is achieved as a result of the sublinear responsivity of these devices. This performance is competitive with consumer image sensors, which show EQEs below 100% and dynamic ranges of ~ 70 dB (ref. 22).

Results and discussion

Phototransistor device architecture and characterization. The channel architecture of the phototransistor is essential for maximizing photodetector performance. Phototransistors using only a BHJ channel have been shown to exhibit broad absorption spectra³⁴, but the disordered nature of BHJs makes it difficult to approach mobilities of $1 \text{ cm}^2 \text{ V}^{-1} \text{ s}^{-1}$ (ref. 27). Conventional high-mobility semiconductors such as dinaphtho[2,3-*b*:2',3'-*f*]thieno[3,2-*b*]thiophene (DNTT)^{18,29} and various metal oxides³⁵ operate as phototransistors, but their photonic performance is limited by low absorption outside the ultraviolet region due to their wide bandgaps. On the other hand, the properties of these devices can be combined by forming a heterojunction between a good absorber that efficiently generates electron-hole pairs and high-mobility semiconductor to rapidly transport the carriers out of the device^{19,28,36,37}. Organic BHJs and high-mobility organic heterostructures have been demonstrated for light-emitting transistors^{38,39}, but no studies have been carried out on photodetectors such as phototransistors, to the best of our knowledge. The channel of our device (Fig. 1c) is composed of DNTT thermally evaporated on top of printed poly(*N*-9'-heptadecanyl-2,7-carbazole-alt-5,5-(4',7'-di-2-thienyl-2',1',3'-benzothiadiazole)): [6,6]-phenyl- C_{71} -butyric acid methyl ester (PCDTBT:PC₇₁BM), a broad-absorption BHJ with high internal quantum efficiency⁴⁰. Thermal evaporation also circumvents the lack of organic

semiconductor solvents orthogonal to PC₇₁BM (ref. 41). It is energetically favourable for photogenerated holes in the highest occupied molecular orbital (HOMO) of PCDTBT to enter DNTT, while electrons are trapped in PC₇₁BM due to the high lowest unoccupied molecular orbital (LUMO) of DNTT. This charge carrier selectivity ensures high photoconductive gain, which is dependent on the ratio of minority carrier lifetime (electron, τ_n) to the transit time of the majority carrier (hole, τ_i). The heterojunction channel is deposited on top of PEDOT:PSS source-drain electrodes printed on a flexible plastic substrate using surface-energy-patterned doctor blade coating, previously developed for organic TFTs (ref. 42). A fluoropolymer gate dielectric is blanket-coated over the whole substrate with aluminium forming the gate electrode. Figure 1d shows the final schematic of the device with a defined channel width and length of 650 μm and 80 μm , respectively.

The phototransistor channel film quality and quasi-static performance are assessed before implementation as an image-sensing pixel. Figure 2a shows the out-of-plane X-ray diffraction (XRD) intensity profile of the DNTT film on top of the BHJ. The peaks at 5.9°, 10.95° and 16.4° are well matched to the (001), (002) and (003) peaks, respectively, as previously reported for high-mobility DNTT films⁴³. A transfer characteristic for a typical device in the dark shown in Fig. 2b exhibits a saturation mobility of $1.38 \text{ cm}^2 \text{ V}^{-1} \text{ s}^{-1}$, an on-off ratio of 1×10^5 , and very little hysteresis. These devices also have a close fit to the ideal square-law behaviour (Supplementary Fig. 1), validating the use of the square-law model to extrapolate mobility. Multiple TFTs were characterized in the same fashion to examine uniformity across an area of 1.2 cm^2 (as summarized in Fig. 2c), with a transistor yield of 40 out of 41. The mean

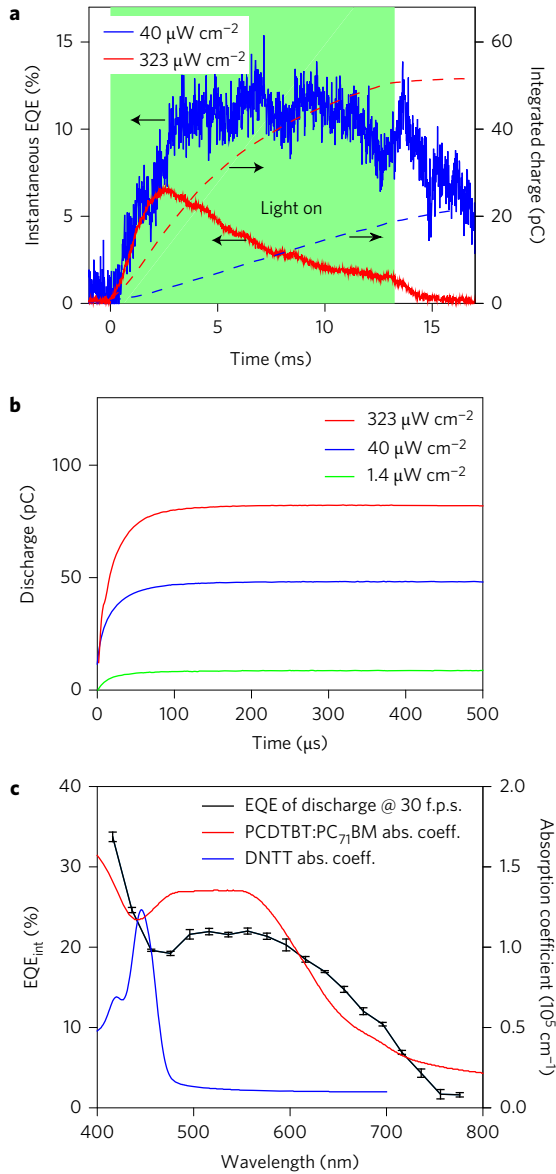


Figure 4 | Phototransistor-based pixel characterization. **a**, Dynamic response of integrating charge and EQE of the rate of integrating charge (labelled 'instantaneous EQE') for the phototransistor-based pixel at irradiances of 40 and 323 $\mu\text{W cm}^{-2}$ at 532 nm. **b**, Dynamic response of the discharge to readout light signals after an integration period of 32 ms for irradiances of 1.4, 40 and 323 $\mu\text{W cm}^{-2}$ at 532 nm. **c**, EQE of integrated charge, labelled 'EQE_{int}' measured at readout from 416 to 784 nm at irradiances varying between 5 and 10 $\mu\text{W cm}^{-2}$ at 30 f.p.s., with error bars signifying the standard deviation of the signal. Also shown are the absorption coefficients of the DNNT and PCDTBT:PC₇₁BM layers of the phototransistor.

and standard deviation saturation mobility, $\log(I_{\text{on}}/I_{\text{off}})$ and threshold voltage are $1.47 \pm 0.16 \text{ cm}^2 \text{ V}^{-1} \text{ s}^{-1}$, 5.25 ± 0.192 and $-2.48 \pm 0.438 \text{ V}$, respectively (see Supplementary Fig. 2 for the threshold voltage histogram). The saturation mobility of these devices is comparable to the value of $2.1 \text{ cm}^2 \text{ V}^{-1} \text{ s}^{-1}$ measured in long-channel (40–50 μm) conventional DNNT TFTs deposited on an *n*-tetradecylphosphonic acid self-assembled monolayer (SAM) with gold top-contact electrodes^{44,45}. This comparable performance and the proper diffraction peaks suggest this BHJ induces crystallization in DNNT, similar to alkyl SAMs (ref. 46), despite an intermediate water contact angle of $81 \pm 7^\circ$ (Supplementary Fig. 3). The output characteristic of a typical device

in the dark and under an irradiance of $40 \mu\text{W cm}^{-2}$ at 532 nm, as well as the EQE, are shown in Fig. 2d. Contact resistance results from a hole barrier of at least 300 meV between the PEDOT:PSS and DNNT imposed by PCDTBT, as seen in Fig. 1c, because this effect is not observed for high-mobility materials deposited directly on PEDOT:PSS (ref. 42). The contact barrier is probably higher than 300 meV, because fullerene-based acceptors have been shown to segregate to the bottom interface⁴⁷. Despite the contact resistance, EQE increases linearly with V_{SD} in the triode region, as described for an ideal photoconductor in equation (1)

$$I_{\text{SD,light}} - I_{\text{SD,dark}} = \Delta I_{\text{SD,light}} = qG_oA \left(\frac{\tau_n}{\tau_t} \right) = qG_oA(\tau_n) \left(\frac{\mu V_{\text{SD}}}{L^2} \right) \quad (1)$$

where q , G_o , μ , A and L are the electron charge (in C), the areal photo-generation rate of electrons in the channel (in $\text{cm}^{-2} \text{ s}^{-1}$), mobility (in $\text{cm}^2 \text{ V}^{-1} \text{ s}^{-1}$), photoactive area (in cm^2), and channel length (in cm), respectively. These devices have high output saturation resistance and an EQE, defined according to equation (2)

$$\text{EQE} = \frac{\Delta I_{\text{SD,light}}}{q\Phi A} \quad (2)$$

where Φ is photon flux (in $\text{cm}^{-2} \text{ s}^{-1}$), above 1,200% at $V_{\text{GS}} = -15 \text{ V}$. Given the EQE of 63% for an OPD using the same BHJ layer as the phototransistor (Supplementary Fig. 4), these devices amplify the photocurrent by up to a factor of 19, and the electron lifetime in the channel is $\sim 80 \mu\text{s}$ in the on state, according to equation (1). The EQE saturates when the device enters the saturation region, because the accumulated carriers at the drain pinch off, fixing the channel voltage drop at higher V_{SD} .

Phototransistor pixel operation and performance. Reading out the integrated photogenerated charge after a frame period, as illustrated in Fig. 1b, has a significantly higher SNR than sampling the instantaneous photocurrent during each row scan. It is optimal for a device to integrate charge in the regime of maximal SNR, which increases for higher light-to-dark current ratio. This ratio is 1.02 and 20 for the phototransistor in the on ($V_{\text{G}} < V_{\text{T}}$) and off ($V_{\text{G}} > V_{\text{T}}$) state, respectively, at $40 \mu\text{W cm}^{-2}$ (Supplementary Fig. 5), making it optimal to integrate charge in the off state. A pixel is created by connecting a biasing capacitor in series with the source of the phototransistor (Fig. 3a) to minimize dark current through the channel and manage parasitic charge injection from overlapping source-gate electrodes. Figure 3b illustrates the mechanisms occurring in the pixel during integration (off state) and discharge (on state) for a rolling shutter addressing scheme. An external charge amplifier is connected to the drain of the phototransistor to monitor charge output and place the drain at virtual ground. The biasing capacitor compensates for the change of charge in the source electrode when the device is switched to the integration mode, which biases $V_{\text{SD}} \cong 5 \text{ V}$ at the start of integration (for calculations see Supplementary Fig. 6). Holes are extracted at the drain upon illumination because $V_{\text{SD}} > 0$, causing a drop in the output voltage of the charge amplifier and leaving behind trapped electrons in the channel. Switching the pixel to the on state discharges the device by injecting holes, which recombine with the trapped electrons in the channel. When the charge retention during integration is high, the amount of integrated charge is equivalent to the discharge during readout.

Examining the photocurrent at the drain electrode during integration provides insights into carrier dynamics not described by

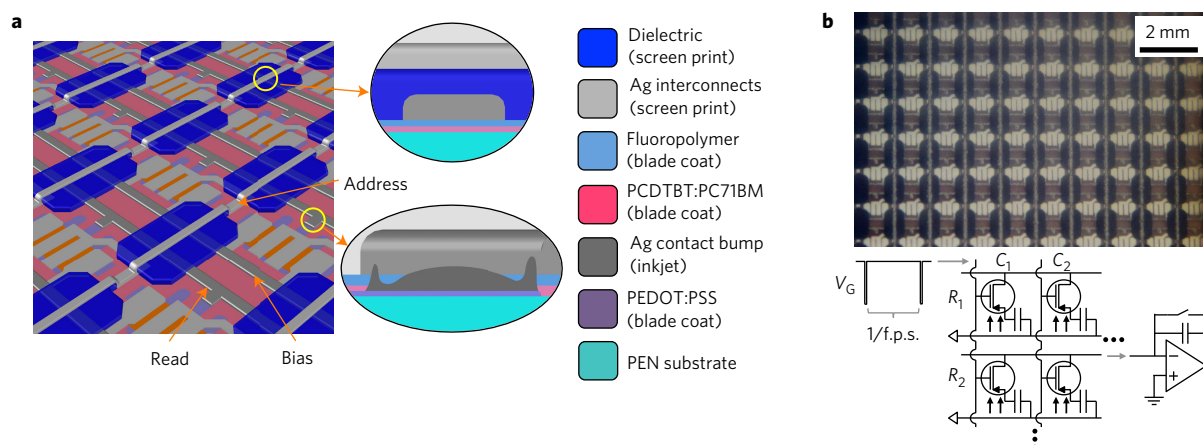


Figure 5 | Phototransistor-based image sensor. **a**, Schematic view of phototransistor-based image sensor with the top and bottom insets showing screen-printed address-readout line overlap and a via interconnect to an underlying drain electrode, respectively. **b**, Optical micrograph of the partially printed image sensor and the associated circuit schematic below.

steady-state phototransistor behaviour^{5,48}. Figure 4a shows the integrated photogenerated charge and the EQE of the rate of integrating charge, labelled ‘instantaneous EQE’, during light exposure for irradiances of $40 \mu\text{W cm}^{-2}$ and $323 \mu\text{W cm}^{-2}$. The instantaneous EQE initially increases at the same rate for both irradiances, which is attributed to the slow transit time of holes to reach the drain due to the lower mobility in the off state. This transit time phenomenon is supported by the continuing collection of charge for several milliseconds after the light source is turned off, as shown in Fig. 4a. Persistence of photocurrent from photoconductive gain is negligible at this timescale because the minority carrier lifetime in the channel is calculated to be $80 \mu\text{s}$ under an irradiance of $40 \mu\text{W cm}^{-2}$. During illumination, the instantaneous EQE peaks at 12 and 7% at $40 \mu\text{W cm}^{-2}$ and $323 \mu\text{W cm}^{-2}$, respectively, before decreasing. The decrease in efficiency with integration time is attributed to the accumulation of electrons in the channel, which increases the probability of recombination with holes. Additionally, instantaneous EQE peaks at higher values at lower irradiances, because the slower rate of electron trapping lowers the probability of recombination. The EQE of the pixel is lower than the peak EQE of the discrete phototransistor because the capacitor blocks direct current flow, thus reducing V_{SD} and in turn photoconductive gain.

Discharge, the phase after integration, is used to read out the amount of integrated charge during a frame period. The discharge dynamics are shown in Fig. 4b for irradiances of 1.4, 40 and $323 \mu\text{W cm}^{-2}$ after an integration time of 32 ms, which corresponds to 30 f.p.s. with a 95% integration duty cycle over the frame period. Over 90% of the integrated charge is discharged in $60 \mu\text{s}$ for all irradiances before settling to a steady output. The similarity of the discharge time to the minority carrier lifetime of $80 \mu\text{s}$ suggests that the injected holes travel quickly through the high-mobility DNTT before recombining with trapped electrons in the channel, as illustrated in Fig. 3b. In addition to fast readout times, high charge retention is desirable during integration to minimize the loss of trapped electrons before discharging. Modulating the readout delay (the time between the end of light exposure and discharge) is a method that can be used to assess the charge retention of a device^{26,30}. It is found that the pixel retains over 99% of the original stored charge for readout delays of 20 ms and 93% for delays of 60 ms (Supplementary Fig. 7). This charge retention enables the total amount of photogenerated charge integrated at video frame rates, with integration periods on the order of 10 to 30 ms, to be accurately determined by reading out the discharge.

Using the rolling shutter scheme in Fig. 3b and reading out the amount of integrated charge through the discharge, the spectral

response of the pixel is measured by the EQE of integrated charge, EQE_{int} , over a period of 30 f.p.s. (32 ms integration time), as shown in Fig. 4c. EQE_{int} is defined in equation (3)

$$\text{EQE}_{\text{int}} = \frac{\text{Photocharge}}{q\Phi t_{\text{int}}A} = \frac{Q_{\text{dis,light}} - Q_{\text{dis,dark}}}{q\Phi t_{\text{int}}A} \quad (3)$$

where photocharge is the difference in pixel discharge under illumination ($Q_{\text{dis,light}}$) and in the dark ($Q_{\text{dis,dark}}$). Integration time (in s) is denoted by t_{int} (see Supplementary Fig. 8 for an analysis on photosensitive regions of the phototransistor pixel). The similarity between the spectrum of EQE_{int} and the absorption spectrum of the BHJ below the absorption cutoff of DNTT shows that the BHJ layer is responsible for photogeneration. A sharp increase in EQE_{int} in the blue-ultraviolet spectrum is attributed to the onset of absorption in DNTT.

Printed imager fabrication and performance

An array of pixels are connected to form an image sensor that is addressable by the gate electrodes in each column to control charge integration and discharge with charge readout through the drain electrodes and large overlap capacitance from the gate dielectric are circumvented by screen-printing separate metal and dielectric layers on top of a discrete array of pixels (Fig. 5a). The sheet resistance of the screen-printed lines ($0.1 \Omega \square^{-1}$) and address-read line overlap capacitance (0.2 nF cm^{-2}) are far lower than those of the printed source-drain electrodes and gate dielectric ($1 \text{ k}\Omega \square^{-1}$ and 10.6 nF cm^{-2} , respectively). Read lines are connected to the drain electrodes buried under the gate dielectric via inkjet-printed silver bumps that protrude above the surface of the gate dielectric, as shown in the inset of Fig. 5a. A micrograph of the fully assembled array and circuit diagram depicting addressing (column) and readout (row) are shown in Fig. 5b.

The dynamic range and EQE_{int} at various frame rates are used as figures of merit to quantify pixel performance. The integrated charge, as determined by the pixel’s charge readout $150 \mu\text{s}$ after discharge as a function of irradiance at 532 nm is shown in Fig. 6a for 5, 30 and 100 f.p.s. with a 95% integration time duty cycle. The noise floor is taken as the standard deviation of the readout dark charge and is independent of frame rate. Lower frame rates integrate more charge at a given irradiance, because the integration time is longer, giving a higher SNR and decreasing the irradiance at which the integrated signal equals the noise floor (noise-equivalent power). For low lighting, ranging from 10 nW cm^{-2} to several $\mu\text{W cm}^{-2}$, the integrated

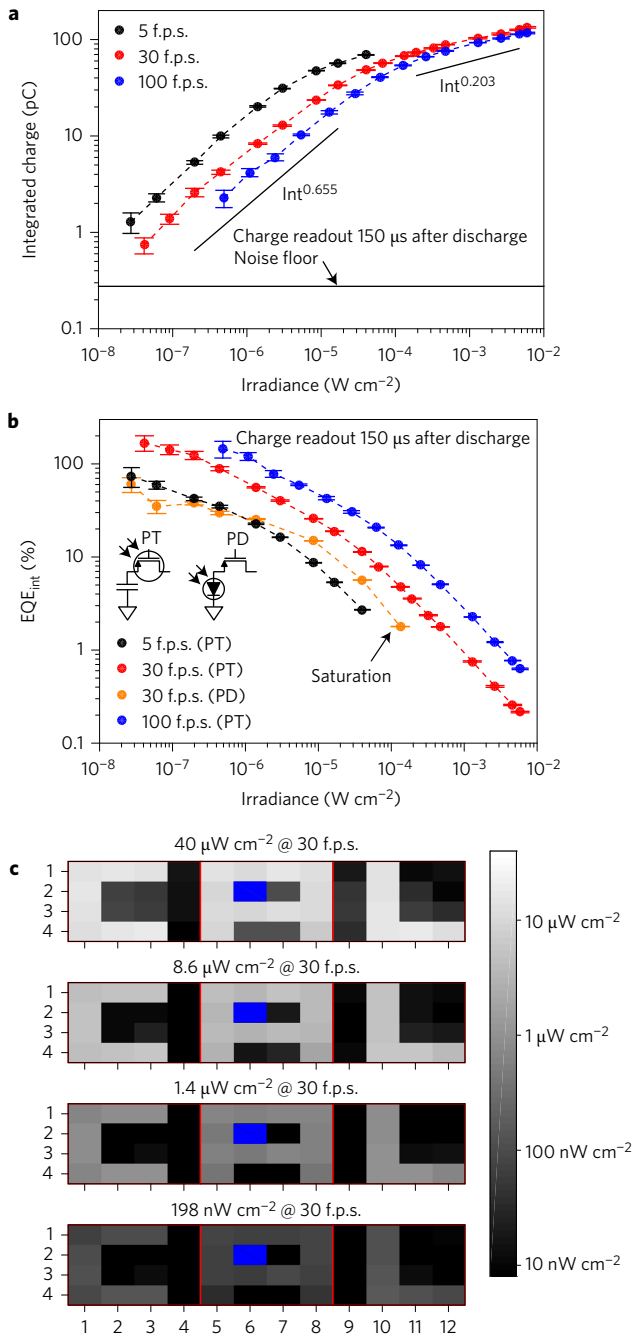


Figure 6 | Phototransistor-based image sensor characterization.

a, Dynamic range of the readout signal from a phototransistor pixel in the image sensor measured at 5, 30 and 100 f.p.s. with a 95% integration time duty cycle for light at 532 nm. Error bars represent standard deviation of the signal. **b**, EQE of integrated charge measured at readout for dynamic range measurements in **a** from a phototransistor pixel (PT) and a photodiode pixel (PD). **c**, Images taken of the letters 'C', 'A' and 'L' through a shadow mask at various background irradiances across separate 4×4 pixel image sensors at 30 f.p.s. A 95% integration time duty cycle is used and charge is readout 150 μ s after discharge. The blue pixel is a defective pixel.

charge increases with irradiance by the power of 0.655 for all measured frame rates. This power law decreases to 0.203 at higher irradiances, which is indicative of the onset of an additional recombination mechanism at high carrier densities. The sublinear response of the pixel enables a wide dynamic range because it prevents saturation of the pixel or readout circuitry at high irradiances, as explained in

Fig. 1a. As a result of this response characteristic, the dynamic range of irradiance measured by the pixel is at least five orders of magnitude, or 103 dB, calculated according to equation (4), at 30 f.p.s.:

$$\text{Dynamic range} = 20 \log_{10} \left(\frac{Irr_{\max}}{Irr_{\min}} \right) \text{dB} \quad (4)$$

In comparison, a conventional charge-integrating photodiode pixel architecture composed of a photodiode in series with a transistor^{9,23,25} made of the same material set as the phototransistor has a dynamic range of 64 dB at 30 f.p.s., which is similar to the 70 dB of consumer-grade CMOS sensors²² (see Supplementary Fig. 9 for photodiode-based pixel architecture and performance). Figure 6b shows EQE_{int} of the phototransistor pixel (PT) measurements in Fig. 6a and a photodiode pixel (PD) at 30 f.p.s. for comparison. The efficiency decreases with longer integration times (lower f.p.s.) and higher irradiances, because the build-up of electron density in the channel increases the probability of recombination with holes, as previously discussed with regards to Fig. 4a. Photoconductive gain is enabled by stored charge in the biasing capacitor of the phototransistor pixel that is injected into the channel and results in EQE_{int} values above 100% at low irradiances. In comparison, the photodiode pixel is limited to the EQE of the photodiode at low irradiances, which is 63% (Supplementary Fig. 4). The phototransistor pixel is also more efficient than the photodiode pixel across its dynamic range, which ends at the saturation of the photodiode's well capacity (see Supplementary Fig. 9 for the dynamic range plot). The decrease in the phototransistor pixel's EQE_{int} with increasing irradiance creates the sublinear responsivity of these pixels, resulting in wide dynamic range.

Image quality was characterized by reading out the integrated charge from pixels driven through address lines for projection-based images of three letters imaged on separate arrays. Figure 6c shows the images taken at various background lighting intensities at 30 f.p.s. calibrated according to the response in Fig. 6a. The photoresponse non-uniformity, which is the ratio of the standard deviation to mean integrated charge for illuminated pixels in the array, is 19% at 198 nW cm^{-2} and 15% at higher irradiances. This low variability results in good uniformity within both illuminated and dark regions. Image lag, the persistence of a light signal from a pixel in frames after the light source is turned off, was measured at 30 f.p.s., as shown in Supplementary Fig. 10. The measured irradiance decreases to 10% of the original value one frame (33 ms) after the light source is extinguished and to 1% after six frames (200 ms).

Conclusion

Image sensors using a novel phototransistor architecture composed of an organic BHJ-high-mobility semiconductor heterojunction are demonstrated in this work. The proven synergy of these two material systems can open new avenues of devices and systems research. Efficient intra-pixel integration of photogenerated charge and fast discharging enables imaging arrays of these devices to be operated between 5 and 100 f.p.s. with EQE_{int} above 100% at low irradiances. In addition, the dynamic range of at least 103 dB measured at 30 f.p.s. exceeds that of the control photodiode pixel²². Finally, these devices were fabricated without photolithography using scalable mass production techniques, opening the possibility of ubiquitous, inexpensive and high-performance imaging systems.

Methods

Methods and any associated references are available in the [online version of the paper](#).

Received 23 August 2016; accepted 17 January 2017; published online 20 February 2017

References

- Arias, A. C., MacKenzie, J. D., McCulloch, I., Rivnay, J. & Salleo, A. Materials and applications for large area electronics: solution-based approaches. *Chem. Rev.* **110**, 3–24 (2010).
- Khan, Y., Ostfeld, A. E., Lochner, C. M., Pierre, A. & Arias, A. C. Monitoring of vital signs with flexible and wearable medical devices. *Adv. Mater.* **28**, 4373–4395 (2016).
- Ostfeld, A. E., Gaikwad, A. M., Khan, Y. & Arias, A. C. High-performance flexible energy storage and harvesting system for wearable electronics. *Sci. Rep.* **6**, 26122 (2016).
- Adrien, P. & Ana Claudia, A. Solution-processed image sensors on flexible substrates. *Flexible Printed Electron.* **1**, 043001 (2016).
- Baeg, K.-J., Binda, M., Natali, D., Caironi, M. & Noh, Y.-Y. Organic light detectors: photodiodes and phototransistors. *Adv. Mater.* **25**, 4267–4295 (2013).
- Jansen-van Vuuren, R. D., Armin, A., Pandey, A. K., Burn, P. L. & Meredith, P. Organic photodiodes: the future of full color detection and image sensing. *Adv. Mater.* **28**, 4766–4802 (2016).
- Pierre, A., Deckman, I., Lechêne, P. B. & Arias, A. C. High detectivity all-printed organic photodiodes. *Adv. Mater.* **27**, 6411–6417 (2015).
- Giuseppina, P., Andrea, G., Marco, S., Dario, N. & Mario, C. Printed photodetectors. *Semicond. Sci. Technol.* **30**, 104006 (2015).
- Ng, T. N., Wong, W. S., Chabinyc, M. L., Sambandan, S. & Street, R. A. Flexible image sensor array with bulk heterojunction organic photodiode. *Appl. Phys. Lett.* **92**, 213303 (2008).
- Takahashi, T. *et al.* Carbon nanotube active-matrix backplanes for mechanically flexible visible light and X-ray imagers. *Nano Lett.* **13**, 5425–5430 (2013).
- Azzellino, G. *et al.* Fully inkjet-printed organic photodetectors with high quantum yield. *Adv. Mater.* **25**, 6829–6833 (2013).
- Deng, W. *et al.* Aligned single-crystalline perovskite microwire arrays for high-performance flexible image sensors with long-term stability. *Adv. Mater.* **28**, 2201–2208 (2016).
- Song, Y. M. *et al.* Digital cameras with designs inspired by the arthropod eye. *Nature* **497**, 95–99 (2013).
- Ko, H. C. *et al.* A hemispherical electronic eye camera based on compressible silicon optoelectronics. *Nature* **454**, 748–753 (2008).
- Kim, J. *et al.* Ultrahigh detective heterogeneous photosensor arrays with in-pixel signal boosting capability for large-area and skin-compatible electronics. *Adv. Mater.* **28**, 3078–3086 (2016).
- Kim, M. *et al.* Flexible organic phototransistors based on a combination of printing methods. *Org. Electron.* **15**, 2677–2684 (2014).
- Li, F. *et al.* Ambipolar solution-processed hybrid perovskite phototransistors. *Nat Commun.* **6**, 8238 (2015).
- Milvich, J. *et al.* Flexible low-voltage organic phototransistors based on air-stable dinaphtho [2,3-*b*:2',3'-*f*]thieno[3,2-*b*] thiophene (DNNT). *Org. Electron.* **20**, 63–68 (2015).
- Liu, X., Lee, E. K., Kim, D. Y., Yu, H. & Oh, J. H. Flexible organic phototransistor array with enhanced responsivity via metal-ligand charge transfer. *ACS Appl. Mater. Interfaces* **8**, 7291–7299 (2016).
- Guo, F. *et al.* A nanocomposite ultraviolet photodetector based on interfacial trap-controlled charge injection. *Nat. Nanotech.* **7**, 798–802 (2012).
- Kang, H.-S., Choi, C.-S., Choi, W.-Y., Kim, D.-H. & Seo, K.-S. Characterization of phototransistor internal gain in metamorphic high-electron-mobility transistors. *Appl. Phys. Lett.* **84**, 3780–3782 (2004).
- Holst, G. C. & Lomheim, T. S. *CMOS/CCD Sensors and Camera Systems* Vol. 408 (JCD Publishing, 2007).
- Street, R. A. *Technology and Applications of Amorphous Silicon* Vol. 37 (Springer, 2000).
- Gelinck, G. H. *et al.* X-ray imager using solution processed organic transistor arrays and bulk heterojunction photodiodes on thin, flexible plastic substrate. *Org. Electron.* **14**, 2602–2609 (2013).
- Rauch, T. *et al.* Near-infrared imaging with quantum-dot-sensitized organic photodiodes. *Nat. Photon.* **3**, 332–336 (2009).
- Zhang, L. *et al.* Large-area, flexible imaging arrays constructed by light-charge organic memories. *Sci. Rep.* **3**, 1080 (2013).
- Xu, H. *et al.* A high-sensitivity near-infrared phototransistor based on an organic bulk heterojunction. *Nanoscale* **5**, 11850–11855 (2013).
- Rim, Y. S. *et al.* Ultrahigh and broad spectral photodetectivity of an organic-inorganic hybrid phototransistor for flexible electronics. *Adv. Mater.* **27**, 6885–6891 (2015).
- Chu, Y. *et al.* Photosensitive and flexible organic field-effect transistors based on interface trapping effect and their application in 2D imaging array. *Adv. Sci.* **3**, 1500435 (2016).
- Nau, S., Wolf, C., Sax, S. & List-Kratochvil, E. J. Organic non-volatile resistive photo-switches for flexible image detector arrays. *Adv. Mater.* **27**, 1048–1052 (2015).
- Lau, P. H. *et al.* Fully printed, high performance carbon nanotube thin-film transistors on flexible substrates. *Nano Lett.* **13**, 3864–3869 (2013).
- Ren, X. *et al.* A low-operating-power and flexible active-matrix organic-transistor temperature-sensor array. *Adv. Mater.* **28**, 4832–4838 (2016).
- Peng, B. *et al.* High performance organic transistor active-matrix driver developed on paper substrate. *Sci. Rep.* **4**, 6430 (2014).
- Han, H. *et al.* Broadband all-polymer phototransistors with nanostructured bulk heterojunction layers of NIR-sensing n-type and visible light-sensing p-type polymers. *Sci. Rep.* **5**, 16457 (2015).
- Ahn, S.-E. *et al.* Metal oxide thin film phototransistor for remote touch interactive displays. *Adv. Mater.* **24**, 2631–2636 (2012).
- Zan, H.-W. *et al.* Amorphous indium-gallium-zinc-oxide visible-light phototransistor with a polymeric light absorption layer. *Appl. Phys. Lett.* **97**, 203506 (2010).
- Qian, C. *et al.* High-performance organic heterojunction phototransistors based on highly ordered copper phthalocyanine/*para*-sexiphenyl thin films. *Adv. Funct. Mater.* **27**, 1604933 (2017).
- Zhang, C., Chen, P. & Hu, W. Organic light-emitting transistors: materials, device configurations, and operations. *Small* **12**, 1252–1294 (2016).
- Capelli, R. *et al.* Organic light-emitting transistors with an efficiency that outperforms the equivalent light-emitting diodes. *Nat. Mater.* **9**, 496–503 (2010).
- Park, S. H. *et al.* Bulk heterojunction solar cells with internal quantum efficiency approaching 100%. *Nat. Photon.* **3**, 297–U295 (2009).
- Gaikwad, A. M. *et al.* Identifying orthogonal solvents for solution processed organic transistors. *Org. Electron.* **30**, 18–29 (2016).
- Pierre, A. *et al.* All-printed flexible organic transistors enabled by surface tension-guided blade coating. *Adv. Mater.* **26**, 5722–5727 (2014).
- Wang, X., Parrish, K. D., Malen, J. A. & Chan, P. K. L. Modifying the thermal conductivity of small molecule organic semiconductor thin films with metal nanoparticles. *Sci. Rep.* **5**, 16095 (2015).
- Zschieschang, U. *et al.* Dinaphtho[2,3-*b*:2',3'-*f*]thieno[3,2-*b*]thiophene (DNNT) thin-film transistors with improved performance and stability. *Org. Electron.* **12**, 1370–1375 (2011).
- Kuribara, K. *et al.* Organic transistors with high thermal stability for medical applications. *Nat. Commun.* **3**, 723 (2012).
- Kobayashi, S. *et al.* Control of carrier density by self-assembled monolayers in organic field-effect transistors. *Nat. Mater.* **3**, 317–322 (2004).
- Campoy-Quiles, M. *et al.* Morphology evolution via self-organization and lateral and vertical diffusion in polymer: fullerene solar cell blends RID C-1209-2008 RID F-6068-2011. *Nat. Mater.* **7**, 158–164 (2008).
- Hamilton, M. C., Martin, S. & Kanicki, J. Thin-film organic polymer phototransistors. *IEEE Trans. Electron. Dev.* **51**, 877–885 (2004).

Acknowledgements

This work was supported in part by the NSF Graduate Fellowship Research Program (grant no. DGE-1106400). This work was also supported in part by Systems on Nanoscale Information fabriCs (SONIC), one of the six SRC STARnet Centers, sponsored by MARCO and DARPA. The authors thank DuPont for provision of polyethylene naphthalate substrates, R. Karim for inkjet printing optimization and A. Javey and V. Subramanian for giving access to equipment in their laboratories.

Author contributions

A.P. fabricated and characterized the device and image sensor. A.G. examined the material properties of the device. A.P. and A.C.A. prepared the manuscript.

Additional information

Supplementary information is available in the online version of the paper. Reprints and permissions information is available online at www.nature.com/reprints. Correspondence and requests for materials should be addressed to A.P.

Competing financial interests

The authors declare no competing financial interests.

Methods

Phototransistor device fabrication. A $90 \times 105 \text{ mm}^2$ polyethylene naphthalate (DuPont Teijin, PQA1) substrate was rinsed in isopropanol and blow-dried. The substrate was then exposed to air plasma (Tegal, Plasmod) for 10 s before being exposed to (heptadecafluoro-1,1,2,2-tetrahydrodecyl)trichlorosilane (Gelest, SIH5841.0) for 20 min under a vacuum of ~ 0.1 – 1 torr to render the substrate hydrophobic. A stainless-steel stencil (fabricated at Photo Etch Technology) with openings was placed on the substrate then exposed to oxygen plasma for 1.2 min at 20% power at 0.2 mbar (Diener, Nano) to create hydrophilic regions for the source and drain. A channel length of $80 \mu\text{m}$ gave excellent process yield⁴². A $35 \mu\text{l}$ volume of PEDOT:PSS (Sigma Aldrich, 739316-25G) diluted 50 vol% in Milli Q water was dispensed in a hydrophilic reservoir at the top of the array. The ink was coated over the substrate by a motor-controlled blade coater (Zehntner, ZUA 2000.60) to a height of $100 \mu\text{m}$ and with a speed of 1 cm s^{-1} , selectively wicking into the defined hydrophilic patterns from the previous oxygen plasma. After annealing the substrate in air for 10 min at $120 \text{ }^\circ\text{C}$, silver nanoparticles (Sun Chemical, EMD 5730, $\sim 100 \text{ nm}$ diameter) were inkjet-printed to form contact bumps to the drain (for a pixel) or both source and drain (for a discrete phototransistor), then annealed again in air for 10 min at $120 \text{ }^\circ\text{C}$. After rendering the substrate hydrophilic by exposure to air plasma for 10 s, PCDTBT (St-Jean PhotoChimie, $M_n = 6 \text{ kDa}$):PC₇₁BM (concentration of 5 mg ml^{-1} : 15 mg ml^{-1}) in chlorobenzene was blanket-coated over the substrate by the motor-driven blade coater in a nitrogen glove box at a blade height of $200 \mu\text{m}$, speed of 3 cm s^{-1} and platform temperature of $40 \text{ }^\circ\text{C}$. The substrate was left to dry on the hotplate at $40 \text{ }^\circ\text{C}$ for an hour before thermally evaporating 20 nm of DNTT through a stencil at a base pressure of 2×10^{-5} torr and deposition rate of 1.5 \AA s^{-1} . This layer defined an effective channel width of $650 \mu\text{m}$, or $325 \mu\text{m}$ in each of the two interdigitated channels. The phototransistor and capacitor dielectric was formed by blade-coating (Zehntner 2040.6050) $100 \mu\text{l}$ of amorphous fluoropolymer (DuPont, AF) diluted to 20 vol% in FC770 (Sigma Aldrich) over the substrate at a speed of 1.5 cm s^{-1} and blade height of $100 \mu\text{m}$, yielding a thickness of 160 nm . The gate and top capacitor electrodes were formed by thermally evaporating 60 nm of aluminium through a stencil at a base pressure of 2×10^{-5} torr and deposition rate of 3 \AA s^{-1} . This completed the array of discrete phototransistors and phototransistor-based pixels. A pictorial description of the process flow is provided in Supplementary Fig. 11.

Array fabrication. An array of discrete devices was connected together by printing conductive (Creative Materials, 118-09A/B) and dielectric material (Creative Materials, 118-08) layers using an industrial-grade screen printer (ASYS, ASP 01M). Read and capacitor bias conductive lines were first screen-printed on the substrate after exposing the substrate to air plasma for 5 s (Tegal, Plasmod). The capacitor bias line connected to the top electrode of the capacitor and the read line connected to the drain electrode via the protruding inkjet-printed contact bump. A dielectric layer was then printed over portions of the first conductive layer before printing the address lines, which connected to the gate of the phototransistors. Each printing step was performed at speed of 10 cm s^{-1} , a snap-off distance of 2 mm and a pressure of 20 N with a substrate post-anneal at $120 \text{ }^\circ\text{C}$ for 5 min in a glove box.

Pixel testing. A custom-made input-output board was designed, as shown in Supplementary Fig. 13, to address and read a pixel. The drive signal and bias capacitor voltage were outputted from a USB-powered function generator (Diligent, Analog Discovery) then amplified by a factor of -4 using an inverting amplifier configuration (Analog Devices, AD 822). During imaging, the capacitor bias was held at a constant 10 V and the address lines were driven at a 95% integration duty cycle with an off- and on-state voltage of 6 and -14 V , respectively. The pixel's charge output was integrated using a resettable charge amplifier (Burr Brown, IVC 102) controlled by the Analog Discovery. Photogenerated charge was extracted by subtracting the charge output of the pixel in the dark from the output under constant illumination. This amplifier also placed the drain of the phototransistor at virtual ground. The outputs of the instrumentation and charge amplifiers were read out by the digital oscilloscope of the Analog Discovery.

The dynamic charge integration response (Fig. 4a) of the pixel was measured by pulsing light for 13 ms during integration. The current from the pixel was used to determine the instantaneous EQE during integration. The spectral response (Fig. 4c) was measured by using the monochromator of an EQE system (PV Measurements, QEXL) as a light source.

Data availability. The data that support the plots within this Article and other findings of this study are available from the corresponding author upon reasonable request.